Detection of first-order liquid/liquid phase transitions in yttrium oxide-aluminium oxide melts

Greaves, G. N.; Wilding, M. C.; Fearn, S.; Langstaff, D.; Kargl, F.; Cox, S.; Van, Quang Vu; Majérus, O.; Benmore, C. J.; Weber, R.; Martin, C. M.; Hennet, L.

Published in:
Science

DOI:
10.1126/science.1160766

Publication date:
2008

Citation for published version (APA):
Greaves, G. N., Wilding, M. C., Fearn, S., Langstaff, D., Kargl, F., Cox, S., Van, Q. V., Majérus, O., Benmore, C. J., Weber, R., Martin, C. M., & Hennet, L. (2008). Detection of first-order liquid/liquid phase transitions in yttrium oxide-aluminium oxide melts. *Science*, *322*(5901), 566-570. https://doi.org/10.1126/science.1160766

Detection of First Order Liquid-Liquid Phase Transitions in Yttrium Oxide – Aluminium Oxide Melts

G.N. Greaves[1], M.C. Wilding[1], S. Fearn[1], D. Langstaff[1], F. Kargl[1], S. Cox[1], Q. Vu Van[1], O. Majérus[2], C.J. Benmore[3], R. Weber[4], C.M. Martin[5], L. Hennet[6]

Abstract

We combine small angle x-ray scattering (SAXS) and wide angle x-ray scattering (WAXS) with aerodynamic levitation techniques to study *in situ* phase transitions in the liquid state under contactless conditions. At very high temperatures yttria-alumina melts show a first order transition, previously inferred from phase separation in quenched glasses. We show how the transition coincides with a narrow and reversible maximum in SAXS indicative of liquid unmixing on the nanoscale combined with an abrupt realignment in WAXS features related to reversible shifts in polyhedral packing on the atomic scale. We also observed a rotary action in the suspended supercooled drop driven by repetitive transitions – a polyamorphic rotor – from which the reversible changes in molar volume (1.2+/-0.2cm^3) and entropy (19+/-4 J/mol/K) can be estimated.

[1]Centre for Advanced Functional Materials and Devices, Institute of Mathematics and Physics, Aberystwyth University, Aberystwyth SY23 3BZ, UK. [2]Ecole Nationale Supérieure de Chimie de Paris, 11 rue Pierre et Marie Curie, 75231, Paris, France. [3]Advanced Photon Source, Argonne National Laboratory, Argonne, IL 60439, USA. [4]Materials Development Inc., 3090 Daniels Court, Arlington Heights, IL 60004, USA, [5] Synchrotron Radiation Source, STFC Daresbury Laboratory, Warrington, Cheshire, WA4 4AD UK. [6]CNRS-CEMHTI, 1d avenue de la Recherche Scientifique, 45071 Orléans cedex 9, France.

Liquids represent some of the most familiar everyday materials. Recognised by their ability to flow, liquids adopt whatever shape contains them and in suspension form spherical drops. They are the intermediate state between solids and gases, and extend over temperature and pressure up to sharp phase boundaries along which the coexist with the adjacent states. Phase transitions across these boundaries are discontinuous and of first order, involving reversible changes in extensive thermodynamic parameters, such as molar volume ΔV and entropy ΔS. Together these define the slope of the phase boundary $\mathrm{d}T/\mathrm{d}P = \Delta V/\Delta S$, for instance the melting curve that separates the liquid from the crystalline state. Phase boundaries themselves can terminate at critical points if the coexistent phases become indistinguishable, the most well known being the formation of fluids from their liquid and vapour states.

The physics of phase transitions and critical phenomena is extensive (*1*). It also includes the wealth of crystalline phases within the solid state where periodic structures can abruptly transform under pressure and temperature into new crystalline states distinct in density and symmetry (*2*). One of the most exciting developments in liquid state science is the growing evidence for different phases of the same liquid and for phase transitions between them at characteristic temperatures and pressures (*3*-*7*). At first glance such “polyamorphism” is counterintuitive, as diffusion processes in a liquid would appear to result in the same time-averaged aperiodic structure. However, liquids unlike crystals are characterised by temporal and spatial fluctuations in density (*1*). These potentially could be the antecedents for different self-assembled phases distinguished by density and entropy (*7*),

particularly in the metastable supercooled state where liquid flow becomes increasingly viscous with falling temperature or increasing pressure. As the concept of polyamorphism has developed the so called "two state model" (*8, 9*) has proved influential, in defining the phase boundary between a low density liquid (LDL) phase and a high density liquid (HDL) phase straddled by spinodal limits. This is illustrated in Fig. 1. In particular, there is a critical point C on the phase boundary below which the LDL and HDL states coexist and beyond which the liquid is single phase. If C lies at negative pressures a liquid-liquid phase transition between HDL and LDL states is expected at ambient pressure and at a characteristic temperature T_{LL} (Fig. 1).

Speculation about the existence of liquid polyamorphs has its origins in the effort to better explain negative melting curves i.e. $dT/dP<0$ (3, 5, 7-9), for which the fusion of ice is the most familiar (*10*). Even though transitions between polyamorphic states in water have now been well-studied (*3 , 11-15*), controversy still exists as to whether these are truly of first order character (*13, 14*) analogous to phase transitions in the crystalline solid state (*2*), or whether they occur via numerous intermediate glassy states (*12, 15*).

Pairs of polyamorphic phases have been identified in many other amorphous and glassy systems (7, *16*) such as silica (*17*), Si (*18*) and Ge (*19*) and microporous zeolites (*20*). With two exceptions, however, transitions have not been observed in the liquid or supercooled state, other than through computer simulation (*4, 7, 11, 21*). The first of these is liquid phosphorous which exhibits a first order transition above its melting point T_m at positive pressure (*22*) between a low density molecular fluid and a high density network liquid - the fluid and liquid phases separated by a large density

difference $\Delta\rho/\rho$ close to 0.4 (*23*). Secondly, polyamorphic macrosegregation but at ambient pressure has been reported in yttria-alumina melts (24). In this case it occurs in the supercooled state and was explored for miniature specimens close to the glass transition temperature T_g. High and low density states with a density difference $\Delta\rho/\rho$ of ~ 0.04 smaller than in liquid phosphorous were reported, the phase separation being consistent with a first order liquid-liquid transition process. Only *ex situ* studies were possible, however, rapidly quenched glasses being used to avoid crystallisation. The liquid-liquid transition temperature was estimated to rise above T_g with increasing alumina content (*24*). Subsequent studies on larger specimens (*25, 26*), have shown that liquid unmixing is sometimes overtaken by crystallisation, with the formation of glass ceramics (*27, 28*), and in other cases rapid quenching overshoots liquid coexistence, resulting in single phase glasses (*26, 29*) which become polyamorphic on reheating to T_g (*26*).

Recent developments in contactless aerodynamic levitation furnaces offer the opportunity to study liquids *in situ* in the supercooled range (*30*). Suspended on a stream of gas, heterogeneous nucleation from contact with any solid container is avoided. Yttria-alumina has been adopted as the model system to study polyamorphism in the supercooled state. Compositions {$(Al_2O_3)_{100-x}$ $(Y_2O_3)_x$ or AYx} have been chosen to search for liquid-liquid transitions *in situ* at temperatures higher than has been possible in previous *ex situ* studies (*24, 25, 27, 28, 29*) and where full conversion to LDL might be expected (*24*). SAXS/WAXS methods enable structure to be followed at the nano and atomic levels (*31, 32*). The geometry of the aerodynamic levitator furnace adapted for combined x-ray experiments (*SOM Text*) is shown

schematically in Fig. 2A. Data were recorded at temperatures from above the melting point T_m through many hundreds of degrees into the supercooled regime, up to the point of crystallisation T_c (Fig. 1). A selection of SAXS profiles at low and high T are plotted in Fig. 3A for three different supercooled liquids: AY15, AY20 and AY25. Each exhibits a sharp minimum at a wavevector Q_{min}, separating the bottom of the interatomic structure factor $S(Q>Q_{min})$ from small angle scatter $I_{SAXS}(Q<Q_{min})$ which caused by nanostructural inhomogeneities. Both are underpinned by a Q-independent background related to thermal density fluctuations (*1, 6*). The rise in I_{SAXS} as $Q\rightarrow 0$ is indicative of liquid inhomogeneities with a narrower size distribution. Where $S(Q)$ and I_{SAXS} increase modestly with temperature across the whole wavevector range for all three liquids, the behaviour captured for AY20 contains a new feature – a narrow and reversible peak just below 1800K (Fig. 3A) – an additional transient source of inhomogeneity.

Precision liquid structure factors $S(Q)$ for the same three liquids obtained at 2500K with high energy X-rays (Fig. 4A) show compositional trends which can be clearly seen in the difference patterns $\Delta S(Q)$ (Fig. 4A inset); namely, the progressive rise in the principal peak close to 2.2Å^{-1} with increased yttria and the developments in the subsequent broad feature between 3 and 5Å^{-1}. Temperature effects in the supercooled region were explored by combining SAXS (Fig. 3A) with WAXS (Fig. 4B). In particular WAXS from supercooled AY20 alters abruptly and reversibly in the vicinity of 1800K, matching the sharp feature in the SAXS (Fig. 3A).

Whilst the liquid drops levitated extremely stably to a few microns mechanically and thermally to better than 5K over the whole supercooled

range (*SOM Text*), the temperature sometimes became variable close to where reversible nanostructural changes affect SAXS (Fig. 3A) and interatomic changes WAXS (Fig. 4B). Depending on the precise laser alignment (Fig. 2A) highly regular oscillations in temperature were observed in separate experiments around 1800K as illustrated in Fig. 2B, pointing to a repetitive pattern of convection within the drop with a fixed frequency (Fig. S1). Video imaging revealed the supercooled drop revolving through 180° about a horizontal axis *(Movies S1, S2*) at the start of each cycle (Fig. 2B), the movement coinciding with a temperature spike. This unusual behaviour was observed for periods of up to an hour and could be resumed following re-melting (Fig. S1).

The changes in the nanostructural order evident from the SAXS (Fig. 3A) are distinguished in Fig. 3B where $I_{SAXS}Q^2$ data integrated for $Q<Q_{min}$ are plotted between 1500K and 2400K until interrupted by crystallisation. The integrated SAXS is proportional to $\langle\Delta\rho^2\rangle$, the amplitude of thermal fluctuations, which rise slowly with temperature if the isothermal compressibility β_T is reasonably constant (*6*). However, this behaviour is decorated with a sharp maximum for liquid AY20 which we interpret as direct evidence for the coexistence of LDL and HDL states with a density difference $\Delta\rho_{LL}$ at T_{LL}. The peak to background in Fig. 3B is proportional to $\Delta\rho_{LL}^2/\langle\Delta\rho^2\rangle$~2 and the maximum is separated in Fig. 3C and deconvoluted into two components. We attribute these to the decline of the HDL phase x_{HDL} accompanied by the rise in the LDL phase x_{LDL} as the temperature drops and *vice versa*. The peak in $x_{HDL}.x_{LDL}$ is at 1788K. This is 250° higher than

previously reported from *ex situ* experiments (*24*) and indicates that the rise in T_{LL} with increasing alumina is much steeper than can be estimated from the cooling rates of rapidly quenched yttria-alumina glasses (*OLM Text*). The T_{LL} maximum for AY20 (Fig. 3C) has a full width half maximum (FWHM) of 22K. Its narrowness and reversibility are the hallmarks of a first order phase transition (*1*) in the liquid state (8,9), in contrast to the gradual transformation through incremental metastable states proposed by some groups (*12, 15*) for HDA-LDA transitions in glassy water.

With the large Q range available from high energy X-rays, detailed real-space distributions $g(r)$ for the three yttria-alumina liquids at 2500K (Fig. 4C) provide signatures for the various nearest neighbour (Al-O,Y-O) and inter-polyhedral (Al-Y,Y-Y) partial pair distribution functions. In the difference distributions $\Delta g(r)$s (insert Fig. 4C), compositional trends inferred from computer modelling of yttria-alumina glasses (*7*) can be seen far more easily. In particular increasing the yttria content naturally leads to an increase in Y-O and a decrease in Al-O correlations. However, it is also accompanied by an increase in Y-Y correlations, signifying the microsegregation of "modifying" yttria polyhedra occurring within decreasing proportions of the network-like liquid alumina matrix. This clustering of yttria polyhedra is similar to the formation of "channels" that percolate through silicate networks (*6*).

Compositional changes affecting cation-cation correlations at high temperatures can also be seen in $\Delta S(Q)$ for the three liquids (Fig. 4A inset). The principal peak at 2.2 $Å^{-1}$ is mainly due to Al-Y correlations whilst the broad feature centred around 4$Å^{-1}$ is principally related to Y-Y and Al-Y correlations (*7, 26, 33*). On the other hand, $\Delta S(Q)$ in supercooled AY20 at high and low

temperatures is different, and with the above attributions indicates a shift to higher Q for Al-Y correlations, the opposite occurring for Y-Y correlations for the HDL-LDL transition. These changes point to a decrease in average Al-Y distances and an increase in Y-Y distances. The latter is illustrated by the cartoon in Fig. 4B showing a switch from edge to corner-sharing yttria polyhedra for LDL. Molten alumina is largely tetrahedral (6, *30, 33*) with most oxygens present as triclusters (OAl_3), in which case the shortening of Al-Y distances for AY20 between HDL and LDL (Fig. 4B) may be due to the break up of OAl_3 groups. Overall the density is expected to decrease. The movement in the principal peak Q_{max} and its increase in intensity $S(Q_{max})$ through the HDL-LDL transition (Fig. 4A and B) coincides with the growth of the LDL phase x_{LDL} analysed from the maximum in the integrated SAXS data (Fig. 3C). The SAXS/WAXS results (Fig. 3C) therefore show how the switch in interatomic polyhedral packing at 1788K (Fig. 4B) matches the nanostructural changes that occur in density fluctuations (Fig. 3B). The present results for AY20 contradict nanocrystalline models proposed for yttria-alumina phase transformations (*27, 28, 29*) where much larger increases in I_{SAXS} would be expected accompanied by diffraction features in $S(Q)$. Both characteristics are clearly seen in SAXS/WAXS measurements when glass nanoceramics are formed close to the glass transition (*31*) but are absent in these experiments on supercooled yttria-alumina liquids at temperatures well above T_g (Figs. 2 and 3).

We turn now to the dynamic oscillations observed in molten AY20 in the vicinity of 1788K – Fig. 2B, Fig. S1 and Movies S1, S2. A model for this unique stop-go behaviour is outlined in Fig. 2B. We propose that the rotation

of the supercooled drop is driven by the HDL-LDL transition occurring within the levitation nozzle adjacent to the upward flow of gas (Fig. 2A) – a polyamorphic rotor. Whenever $T<T_{LL}$ the liquid within the nozzle (which is approximately one third of the drop – see Movies S1, S2) switches abruptly to LDL. As $\Delta\rho/\rho < 0$ the drop is destabilized resulting in the low density zone at the bottom flipping to the top, the high viscosity of the LDL phase (*26*) maintaining the rigidity of the drop. The unmixing time is at least as short as the frame exposure time (30ms). Taking the flip time τ from the full video sequence *(Movies S1, S2*) gives $\Delta\rho/\rho$=0.031+/-0.004 (*34*), close to the *ex situ* value determined from recovered rapidly quenched material (*26*). From the peak to background in Fig. 3B, the size of thermal fluctuations in yttria-alumina liquids away from the transition $\left\langle \Delta\rho^2 \right\rangle^{1/2}/\rho \sim 0.02$, which is comparable to measurements on supercooled silica (6).

The HDL-LDL increase in molar volume in supercooled AY20 in the nozzle ΔV_{LL} is 1.2+/-0.2cm^3. This initiates the rotation (*Movie S1*), bringing the LDL cap into the laser beam where it switches back to HDL when *T* exceeds T_{LL} (Fig. 2B). In the meantime material at the bottom surrounded by the nozzle gradually cools and when *T* there drops below T_{LL} the HDL-LDL transition repeats and a new cycle commences. Because the HDL-LDL transition is ordering (*26*) this will be accompanied by an exotherm emanating within the material in the nozzle and spreading through to the rest of the drop. However, as soon as the rotor spins the LDL zone under the laser spot (Fig. 2B), the HDL-LDL exotherm should be interrupted by an LDL-HDL endotherm. This qualitatively explains the thermal spike at the start of each cycle where the initial exotherm is overtaken by a sharp dip followed by gradual warming

before the next cycle starts (Fig. 2B). The pyrometer and video brightness fluctuations (*OLM Text*), however, can also be attributed in part to variations in emissivity over the surface adding some uncertainty to the temperatures recorded by the pyrometer. Nevertheless, taking the measured temperature limits from Fig. 2B, a figure for the enthalpy change ΔH_{LL} associated with the polyamorphic transition of 34+/-8kJ/mol is obtained (*34*), similar to the calorimetric value reported from reheating quenched glasses (*26*).

The critical temperature for the "two-state" model (*8*) which is defined by $\Delta H / 2R$, where *R* is the gas constant, is 2030+/-480K. Moreover the HDL-LDL decrease in entropy $\Delta S_{LL} = \Delta H_{LL} / T_{LL}$ is 19+/-4J/mol/K, approximately half the entropy of fusion (*35*), which therefore excludes alternative explanations of liquid-liquid transitions in supercooled yttria-alumina based on crystallisation (*27,28, 29*). ΔS_{LL} and ΔV_{LL} are the first order thermodynamic drivers for the polyamorphic transition and determine the gradient of the HDL-LDL phase boundary in supercooled AY20, viz: $dT / dP = \Delta V_{LL} / \Delta S_{LL}$ = -62°/GPa. This negative slope and the +/-σ limits (Fig. 3C) closely match predictions from the two-state model (Fig. 1) from which a more precise value for the critical point C (1804K, -0.31GPa) is obtained using the Ponyatovsky formalism (*36*).

We believe that the contactless *in situ* approach described here, which has enabled us to detect the variables that define the liquid-liquid transition in supercooled yttria-alumina, can also be applied at lower temperatures to search for polyamorphic and non-equilibrium transitions more generally where ambient pressure is the norm – for instance in other supercooled inorganic systems like liquid metals as well as in organic liquids, Indeed it may well be

possible with levitated drops and SAXS/WAXS to explore instabilities in supercooled water at temperatures which have so far proved inaccessible (*3*).

References

1 A. Onuki, Phase Transition Dynamics (Cambridge University Press, Cambridge, 2004).
2 P. W. Bridgeman, *The Physics of High Pressure* (G.W. Bell & Sons, London, 1949).
3 P. G. Debenedetti, *Metastable Liquids* (Princeton University Press, Princeton NJ, 1997)
4 P. H. Poole, T. Grande, C.A. Angell and P.F. McMillan *Science* **275** 322 (1997).
5 P. F. McMillan *J. Mater. Chem.* **14** 1506 (2004).
6 G. N. Greaves, S. Sen, *Adv. Phys.* **56**, 1 (2007).
7 P. F. McMillan *et al.*, *J. Phys.: Condens. Matter* **19**, 415101 (2007).
8 E. Rapoport, *J. Chem. Phys.* **46**, 3279 (1967).
9 E. G. Ponyatovsky, O. I. Barkalov, *Mater. Sci. Rep.* **8**, 147 (1992).
10 O. Mishima, L. D. Calvert, E. Whalley, *Nature* **310**, 393 (1984).
11 P. H. Poole, F. Sciortino, U. Essmann, H. E. Stanley, *Nature* **360**, 324.
12 J. L. Finney, A. Hallbrucker, I. Kohl, A. K. Soper, D. T. Bowron, *Phys. Rev. Lett.* **88** (2002).
13 O. Mishima, Y. Suzuki, *Nature* **419**, 599 (2002).
14 R. J. Nelmes *et al.*, *Nature Phys.* **2**, 414 (2006).
15 M. M. Koza, R. P. May, H. Schober, *J. Appl. Cryst.* **40**, S517 (2007).
16 19A. V. V. Brazhkin, S. V. Popova and R. N. Voloshin, *High Pressure Res.* **15** 267 (1997)
17 M. Grimsditch, *Phys. Rev. Lett.* **52**, 2379 (1984).
18 PF. McMillan, M. Wilson, D. Daisenberger and D. Machon *Nat. Mater.* **4** 680 (2005).
19 A. Di Cicco, E. Principi, M. Minicucci, S. De Panfilis, A. Filipponi, F. Decremps, F. Datchi, J-P Iti´e, P. Munsch andA. Polian *High Pressure Res.* **24** 93 (2004)
20 G. N. Greaves, F. Meneau, O. Majerus, D. G. Jones, J. Taylor, *Science* **308**, 1299 (2005).
21 S. Sastry and C.A. Angell, *Nature Mater.* **2**, 739 (2003)
22 Y. Katayama *et al.*, *Nature* **403**, 170 (2000).
23 Y. Katayama *et al.*, *Science* **306**, 848 (2004).
24 S. Aasland, P. F. McMillan, *Nature* **369**, 633 (1994).
25 J. K. Weber et al, *J. Am. Ceram. Soc.* **83**, 1868 (2000)
26 M. C. Wilding, P. F. McMillan, *J. Non-Cryst. Solids* **293**, 357 (2001).
27 K. Nagashio, K. Kuribayashi, *J. Am. Ceram. Soc.* **85**, 2353 (2002)
28 J. A. Tangeman, B. L. Phillips, R. Hart, *J. Am. Ceram. Soc.* **90**, 758 (2007)
29 L. B. Skinner, A. C. Barnes, P. S. Salmon, W. A. Chrichton, *J. Phys.: Condens. Matter* **20**, 205103 (2008).
30 C. Landron *et al.*, *Phys. Rev. Lett.* **86**, 4839 (May 21, 2001).
31 W. Bras, G. N. Greaves, M. Oversluizen, S. M. Clark and G. Eeckhaut *Journal of Non-Crystalline Solids* **351**, 2178 (2005)
32 R. J. Cernik *et al.*, *J. Synchrotron. Rad.* **11**, 163 (2004).
33 V. Cristiglio *et al.*, *J. Phys.: Condens. Matter* **19** , 415105 (2007).
34 Equation of motion of an unstable spherical pendulum is $d^2\theta/dt^2 = Q\sin\theta$, where θ is the angular displacement from vertical

and $Q = A(\Delta\rho/\rho)g/a$, a is the radius (1.15mm) and g is the acceleration due to gravity (9.8ms^{-2}). For the polyamorphic rotor model $\Delta\rho/\rho$ is the density contrast between HDL and LDL components of the sphere, A is a constant which governs the moment of inertia and is approximately equal to the fraction of the sphere converted to LDL (~1/3). The time for the sphere to flip through 180° is $\tau \approx 6Q^{-1/2}$. From the video frames τ= 600+/-70ms, giving $\Delta\rho/\rho$ =0.031+/-0.004. If the enthalpy associated with the HDL-LDL transition is emitted radiatively, $dT/dt = \frac{\varepsilon\alpha S(T^4 - T_0^4)}{C_P}$ where ε is the emissivity, σ is Stefan's constant (5.67 10^{-8} Wm^{-2}K^{-4}) and S is the area of the sphere, T_0 is the equilibrium temperature, and the specific heat C_P is set equal to the Dulong and Petit value of 24.96 J/mol. The radiant exotherm is parameterised from the measured temperature limits shown in Fig. 2B, the onset of the equivalent LDL-HDL endotherm being offset by 250ms from the rise of the initial HDL-LDL exotherm that starts the cycle. The resulting oscillating temperatures are shown by the dashed blue curve with the emitted/absorbed powers yielding a value for the enthalpy ΔH_{LL} of the polyamorphic transition of 34+/-8kJ/mol.

35 If alumina or YAG nucleated instead of LDL, as has proposed by some researchers (*27, 28, 29*), the exotherm would be due to ΔS_{fusion} which equals 48kJ/mol/K and 30kJ/mol/K respectively, compared to the ΔS_{LL} value of 19+/-4kJ/mol/K measured in these *in situ* experiments. Also $\Delta\rho/\rho$ >0 which would not destablise the rotor action (Fig. 2B and *Movie S1 and S2*).

36 The measured temperature rise at the top of the rotor, which we attribute to the LDL-HDL transition initiated in the nozzle, indicates significant superheating. We note that this is in excess of the upper spinodal limit shown in Fig. 2B defined by the two-state model (*9*), in which case internal superheating might trigger the reverse endothermic LDL-HDL transition rather than external laser heating.

37 We are grateful for very useful discussions with Wim Bras, Paul McMillan and Peter Poole. The Science Technology Facility Council and staff at the Synchrotron Radiation Source are thanked for access to the SAXS/WAXS facilities on station 6.2 and the Advanced Photon Source for access to high energy x-ray scattering facilities on 11-ID-C. We also acknowledge the support of the Higher Education Funding Council in Wales through the Centre for Advanced Functional Materials and Devices.

Supporting Online Material

SOM Text

Materials and methods

Fig. S1 and Fig. S2

Movies S1 and S2

Figure Captions

Figure 1. *T-P* phase boundary separating HDL and LDL phases surrounded by spinodal limits. Dashed curves: calculations from the two state model (8, 9). Solid curves: $dT/dP = \Delta V_{LL} / \Delta S_{LL}$ is determined from the changes in entropy ΔS_{LL} and molar volume ΔV_{LL} for supercooled AY20, with +/-σ limits taken Fig. 3C. This places the critical point C at 1804K, and -0.31GPa. The melting point T_m and the HDA glass transition temperature T_g for AY20 are also included (*26, 31*), together with the crystallisation temperature T_c taken from Fig. 3B and from rapid quenching (*29*).

Figure 2. A Schematic of the aerodynamic furnace for SAXS/WAXS experiments at the Synchrotron Radiation Source station 6.2 (*32*). Laser and pyrometer are directed downwards on the drop which is supported by aerodynamic drag forces from a vertical stream of argon. ΔT ~50K (*25, 29*). SAXS and WAXS detected as shown using multi-wire proportional counters (*32*). The levitator was adjusted vertically for constant transmission (I_T/I_0) through the drop. **B** Top: 0.25Hz stop-go rotation in vicinity or T_{LL} (see also Fig. S1). Left: Video images A-F illustrating horizontal rotation (*Movies S1, S2*). Centre: Fluctuating image brightness for pixel area shown in frame A compared to pyrometer output for one 4s cycle. 180° rotation takes 600ms after which the bead is virtually stationary. Dashed lines are +/-σ limits from Fig. 3C. Right: Polyamorphic rotor model. HDL-LDL transition occurs repeatedly at the bottom of the sphere whenever $T<T_{LL}$, the mechanical instability causing the LDL zone to rotate to the top where it transforms back

to HDL in the laser beam. Dotted lines follow polyamorphic model (*34*) also shown above for extended sequence.

Figure 3. Small angle X-ray scattering (SAXS) data for supercooled AY15, AY20 and AY25 liquids revealing the intensity of random fluctuations measured at the Synchrotron Radiation Source station 6.2 (*SOM*). **A** Log I_{SAXS} v Log$Q$ plots with a sharp minimum at Q_{min}<0.05Å^{-1} between the rise for Q <Q_{min} and the increase in the structure factor for Q>Q_{min}. Note the rise and fall in I_{SAXS} for AY20 in the vicinity of 1788K. **B** SAXS integrated for Q <Q_{min} $\int_{0.03}^{Q_{\min}} I_{SAXS} Q^2 dQ$, showing the linear temperature rise for the three supercooled liquids. SAXS was followed as far as crystallisation T_c in each case (*SOM*). The sharp peak for AY20 at 1788K identifies a liquid-liquid transition AY20 and AY25 are offset vertically by 1 and 2 respectively. **C** Top: Integrated SAXS $\int_{0.03}^{Q_{\min}} I_{SAXS} Q^2 dQ$ for supercooled AY20 from Fig. 3B with the thermal background removed (——) and deconvoluted into two back-to-back Avrami-like sigmoids, x_{LDL} (-·-·-·) x_{HDL} (- - - -) where $x_{LDL} = e^{-(\frac{T-T_0}{2\Delta T_{LL}})4} = 1 - x_{HDL}$ and T_0=1752K, from which T_{LL}=1788+-9K. Bottom: Discontinuities in the position Q_{max} ■ and intensity $S(Q_{max})$ ○ of the principal peak occurring at 1788K (inset to Fig. 4B) which follow x_{LDL} (-·-·-·-·).

Figure 4. Structure factors $S(Q)$ and distribution functions $g(r)$ for supercooled AY15, AY20 and AY25 liquids. **A** $S(Q)$s measured on 11-1D-C at the Advanced Photon Source with high energy X-rays (*SOM*). Inset: - - - - $\Delta S(Q)$ for pairs of liquids displaying two features annotated with Q values for cation-

cation correlations obtained from computer simulation (*7*). —— $\Delta S(Q)$: the difference between high and low temperature $S(Q)$s for AY20 taken from B, arrows identifying the inter-polyhedral changes ΔQ_{AB} accompanying the HDL-LDL transition. **B** $S(Q)$s fro AY20 at 2392K (■) and 1515K (○) measured on at the Synchrotron Radiation Source station 6.2 (*SOM*) and compared to HEXRD taken from A (———). Inset: Changes to the principal peak with temperature, below 1786K in blue and above 1800K in red, showing the shift in position Q_{max} and intensity $S(Q_{max})$ highlighted in the inset to A and in Fig. 3C identifying the liquid-liquid transition. Cartoon: proposed reversible changes in polyhedral packing between HDL and LDL phases. The LDL inter-cation distances $r_{Al\text{-}Y}$ and $r_{Y\text{-}Y}$ are estimated using $\Delta r_{AB} \sim r_{AB}\Delta Q_{AB} / Q_{AB}$ where ΔQ_{AB} is the HDL-LDL shift in $S(Q)$ AY20 features from B with the HDL Q_{AB} and r_{AB} taken from A and C respectively. **C** $g(r)$s obtained by Fourier transforming $S(Q)$s from A. Inset: $\Delta g(r)$ for each of the pairs of liquids identifying nearest neighbour Al-O, Y-O and O-O separations as well as inter-polyhedral Al-Al, Al-Y and Y-Y correlations, arrows centred on the average distances r_{AB} obtained from simulations (*7*).

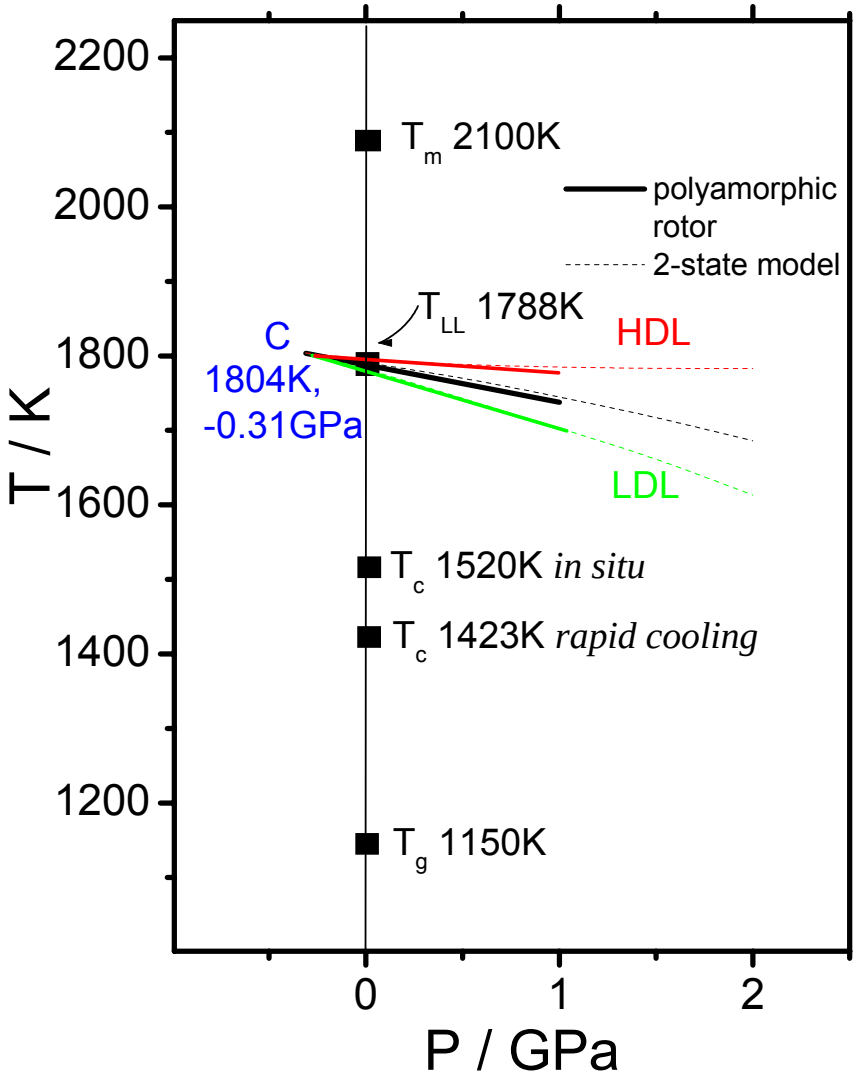
2200
2000
1800
1600
1400
1200
T / K
0
1
2
P / GPa
T_m 2100K
polyamorphic
rotor
2-state model
T_LL 1788K
HDL
C
1804K,
-0.31GPa
LDL
T_c 1520K in situ
T_c 1423K rapid cooling
T_g 1150K

Figure 1

A

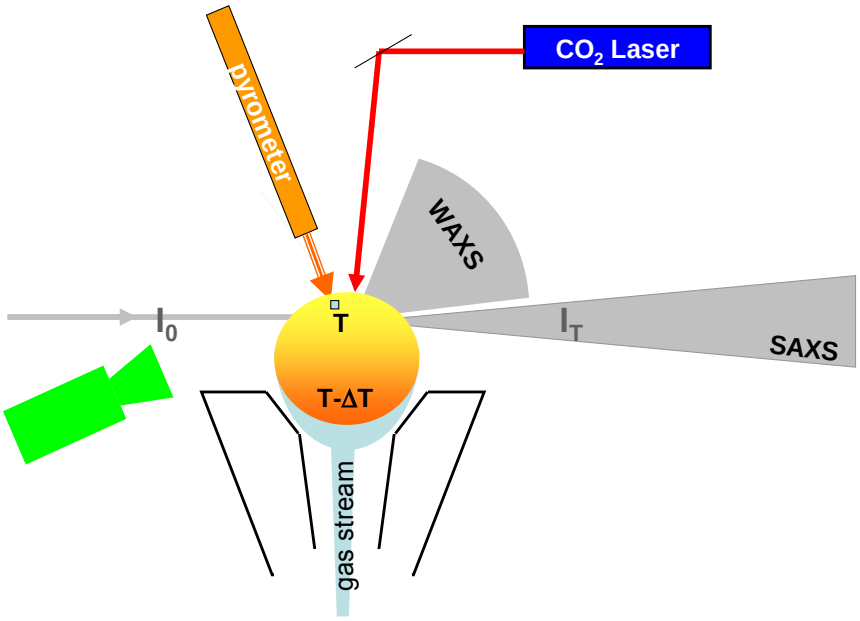

Figure 2

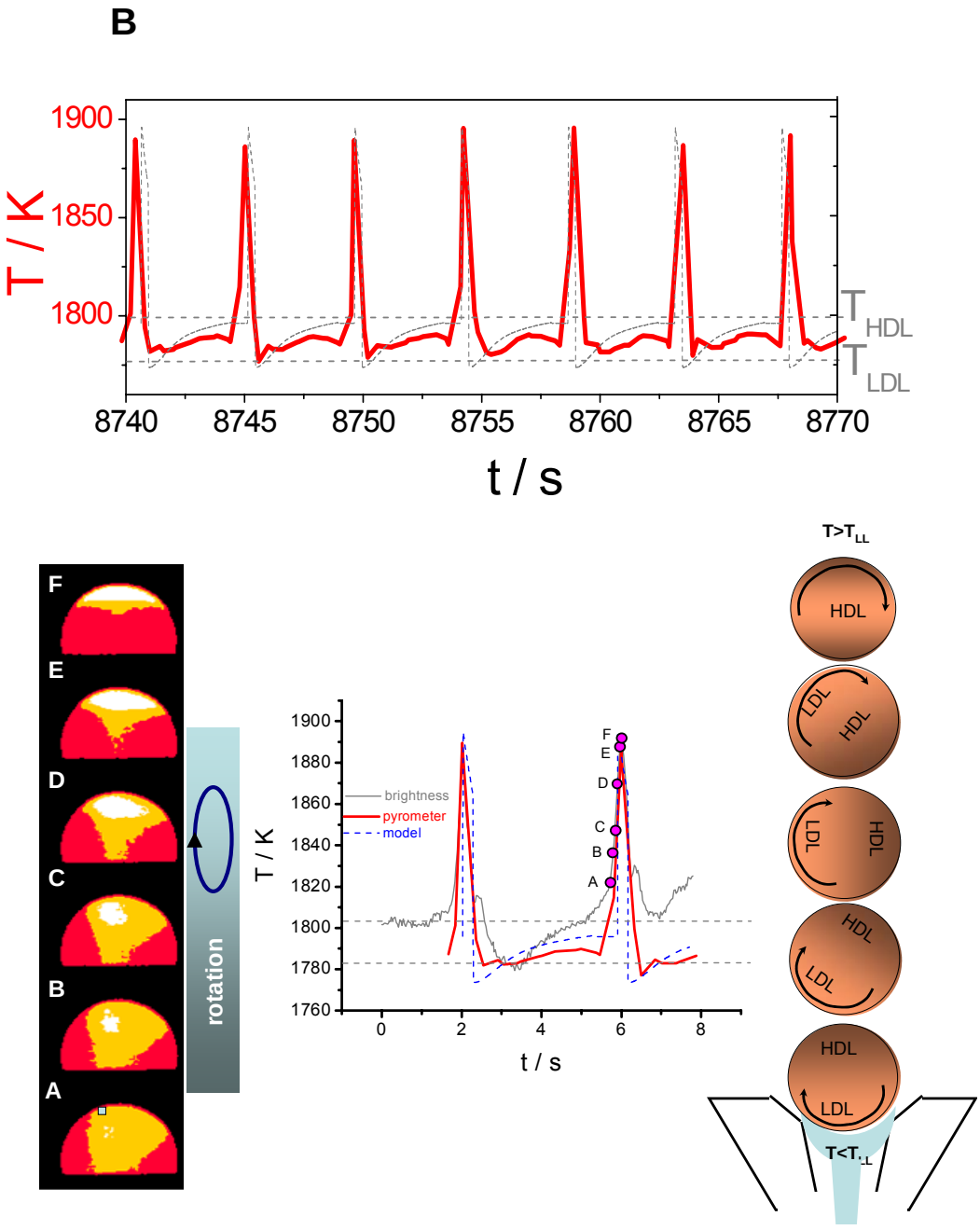
B
1900
1850
1800
T / K
T HDL
T LDL
8740
8745
8750
8755
8760
8765
8770
t / s
F
E
D
C
B
A
rotation
1900
1880
1860
1840
1820
1800
1780
1760
T / K
brightness
pyrometer
model
0
2
4
6
8
t / s
T>T LL
HDL
LDL
HDL
LDL
HDL
HDL
LDL
HDL
LDL
T<T LL

Figure 2

A

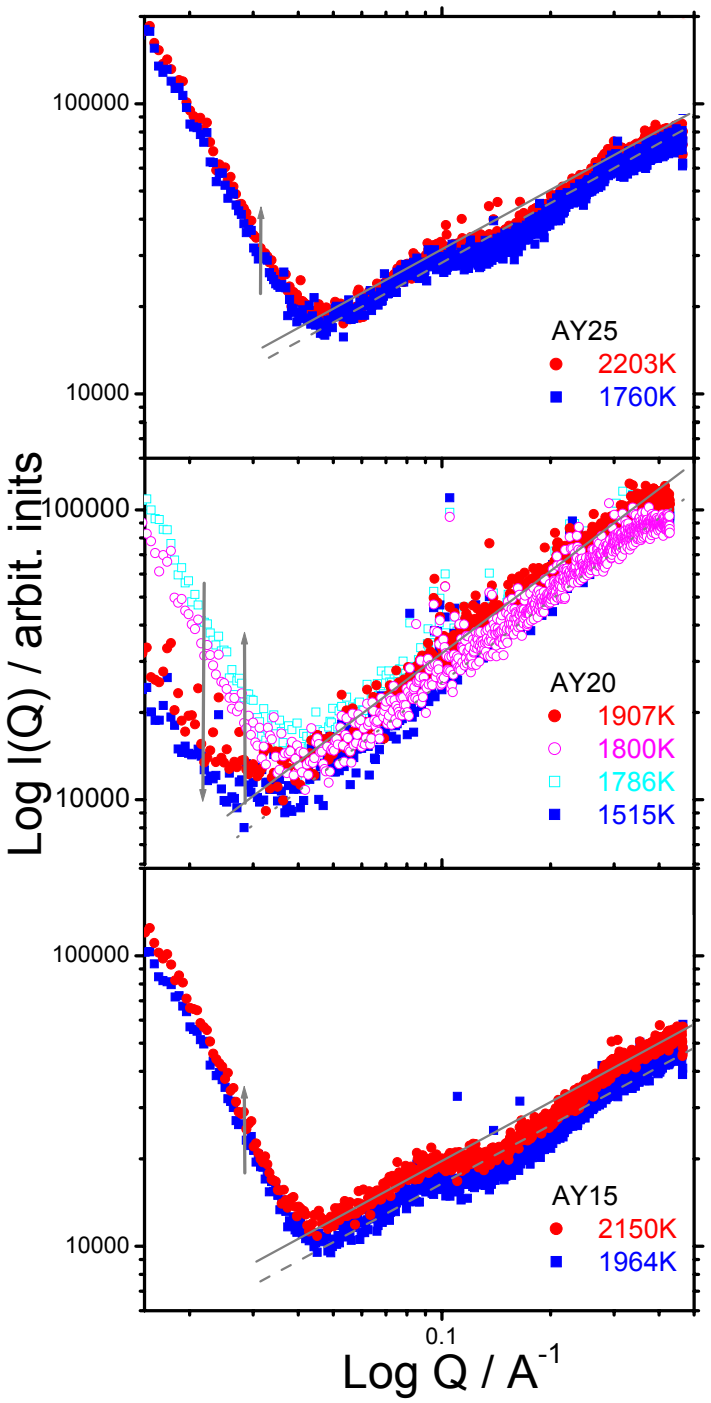
100000
10000
AY25
2203K
1760K
100000
10000
AY20
1907K
1800K
1786K
1515K
100000
10000
AY15
2150K
1964K
Log I(Q) / arbit. inits
0.1
Log Q / A-1

Figure 3

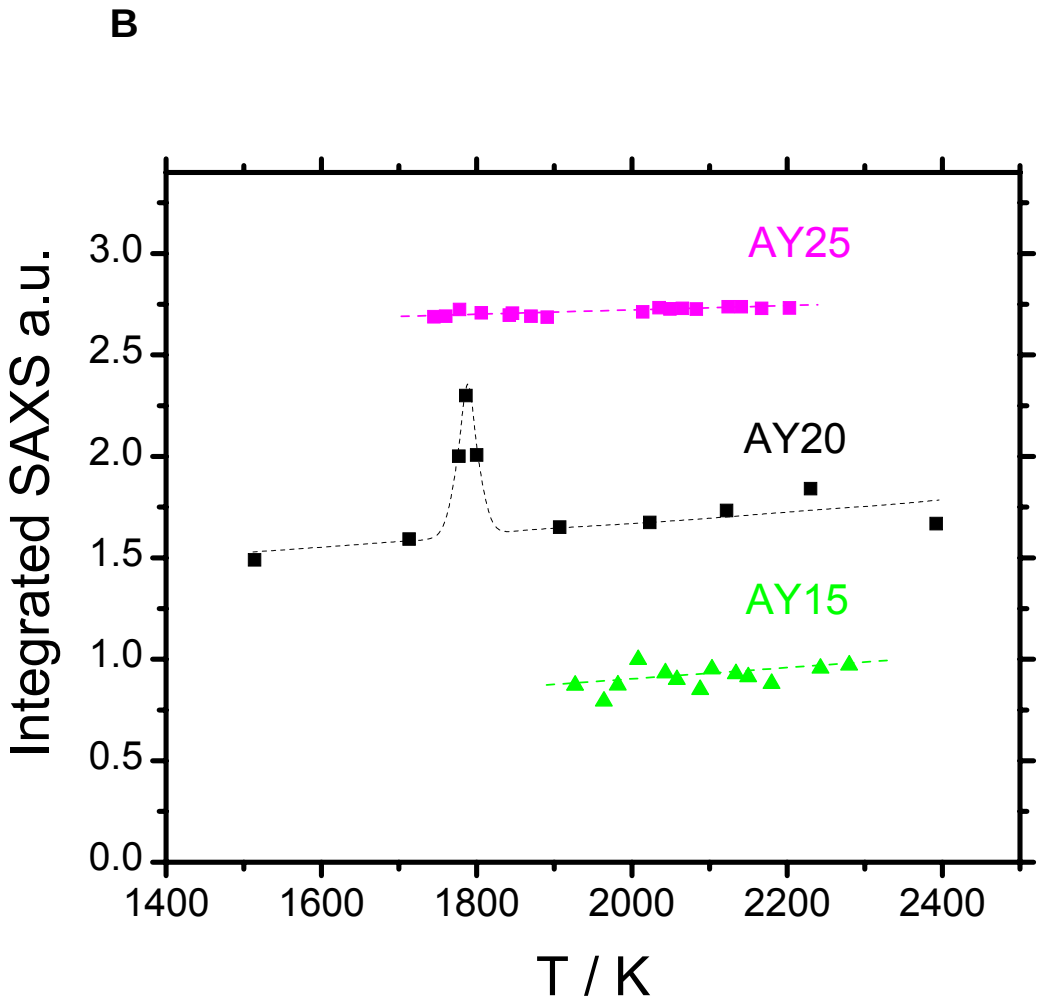
B
Integrated SAXS a.u.
3.0
2.5
2.0
1.5
1.0
0.5
0.0
1400
1600
1800
2000
2200
2400
T / K
AY25
AY20
AY15

Figure 3

c

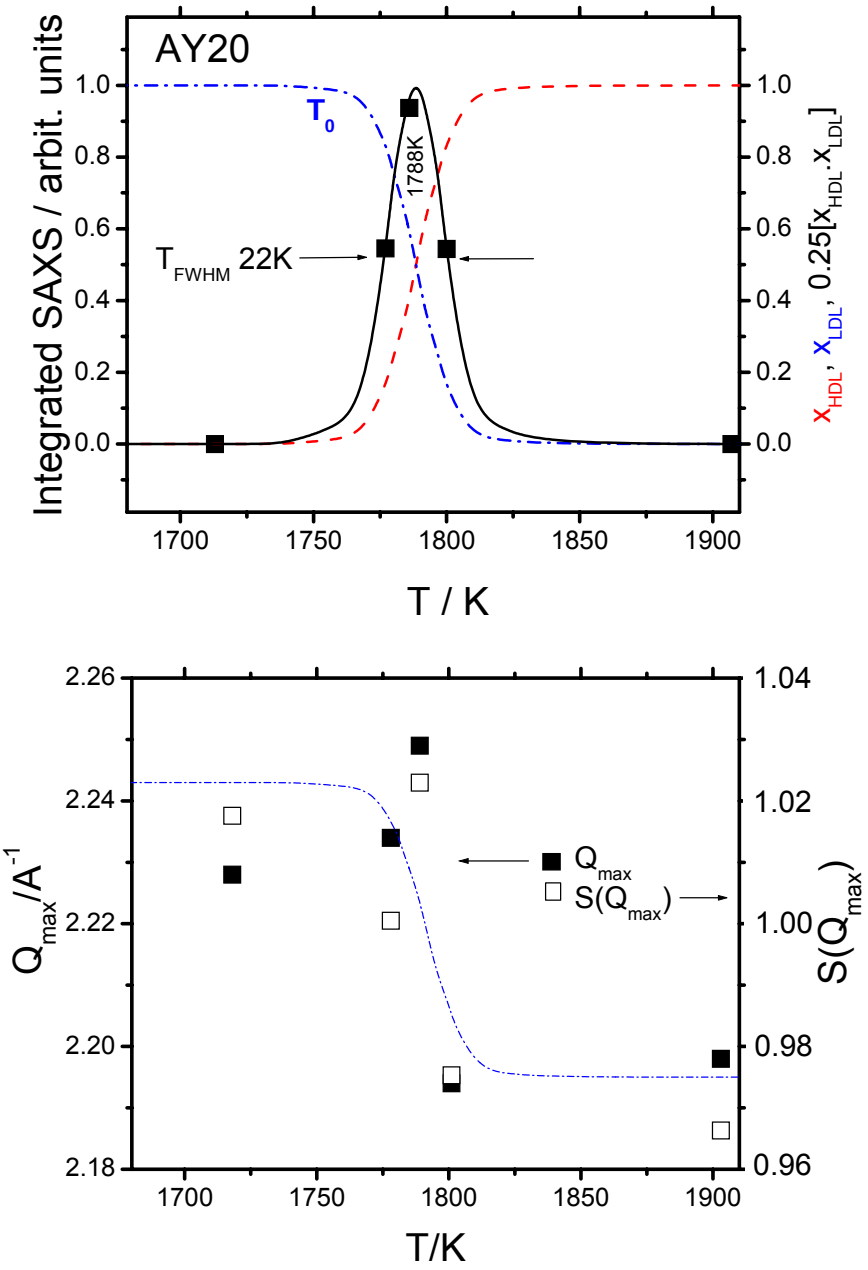
AY20
Integrated SAXS / arbit. units
x_{HDL}, x_{LDL}, 0.25[x_{HDL}.x_{LDL}]
T_0
1788K
T_{FWHM} 22K
T / K
Q_{max}/A^{-1}
$S(Q_{max})$
Q_{max}
$S(Q_{max})$
T/K

Figure 3

A

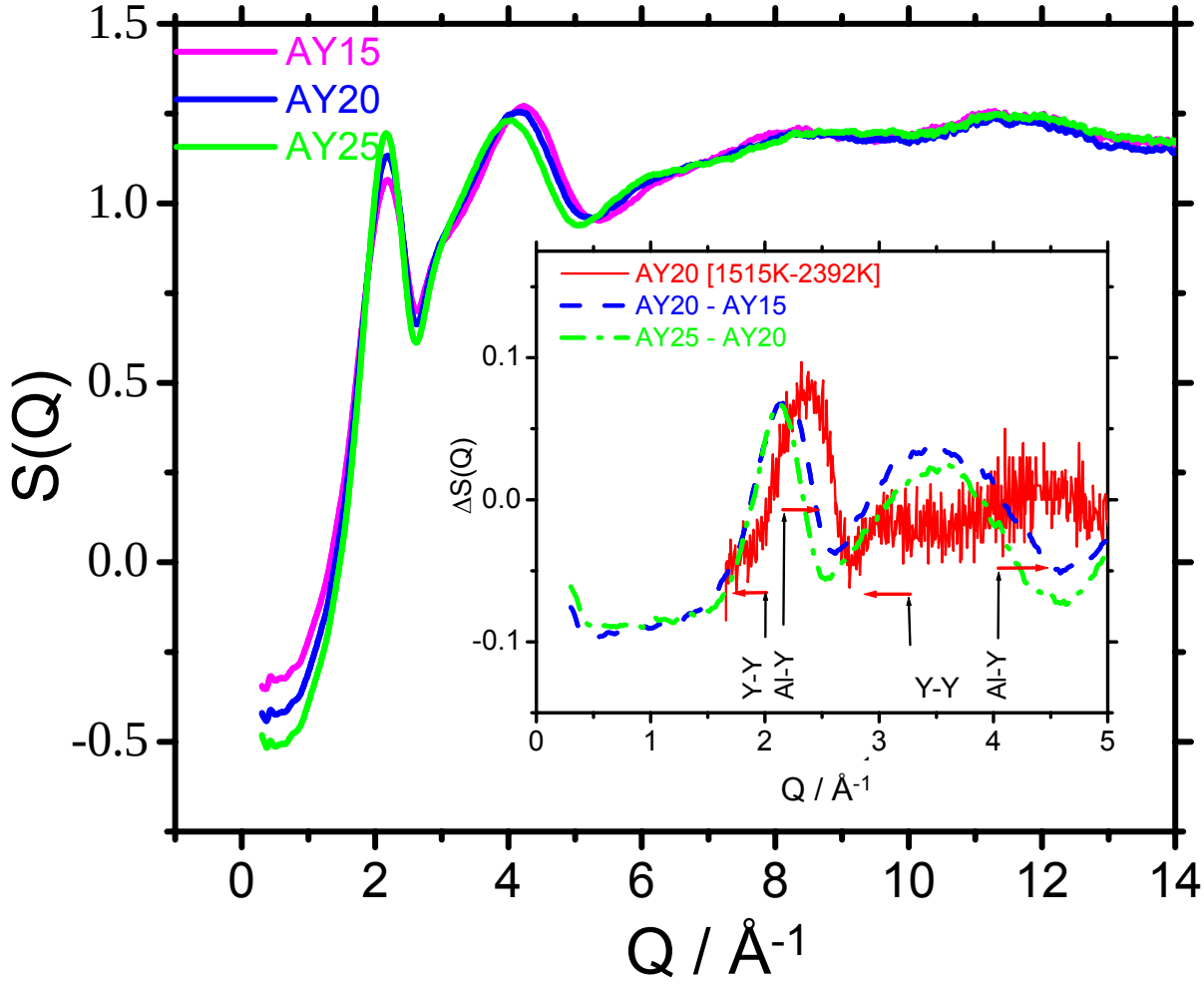
AY15
AY20
AY25
S(Q)
Q / Å-1
AY20 [1515K-2392K]
AY20 - AY15
AY25 - AY20
ΔS(Q)
Y-Y
Al-Y
Y-Y
Al-Y
Q / Å-1

Figure 4

B

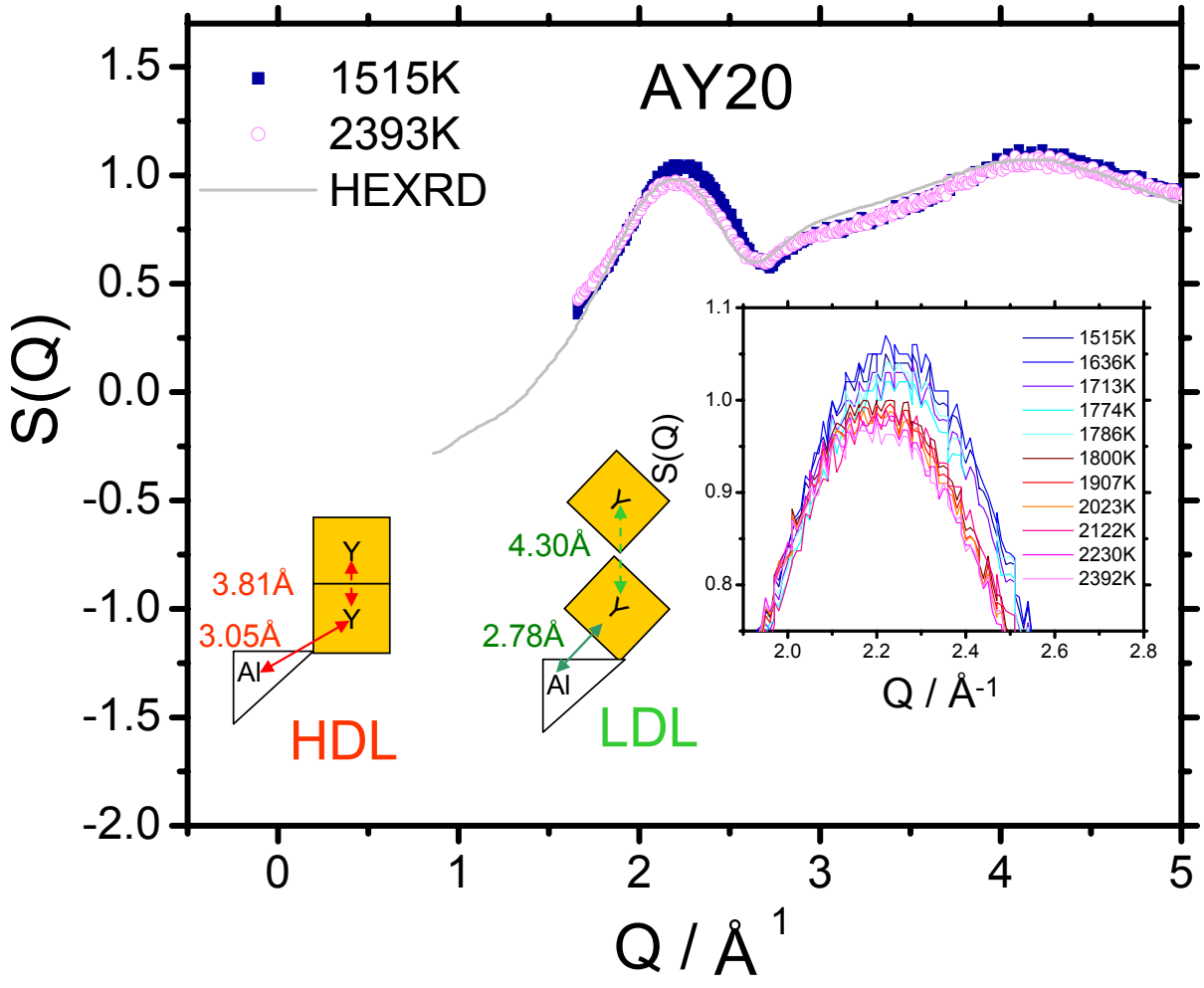
AY20
1515K
2393K
HEXRD
S(Q)
Q / Å 1
3.81Å
3.05Å
Y
Y
Al
HDL
4.30Å
2.78Å
Y
Y
Al
LDL
S(Q)
Q / Å-1
1515K
1636K
1713K
1774K
1786K
1800K
1907K
2023K
2122K
2230K
2392K

Figure 4

c

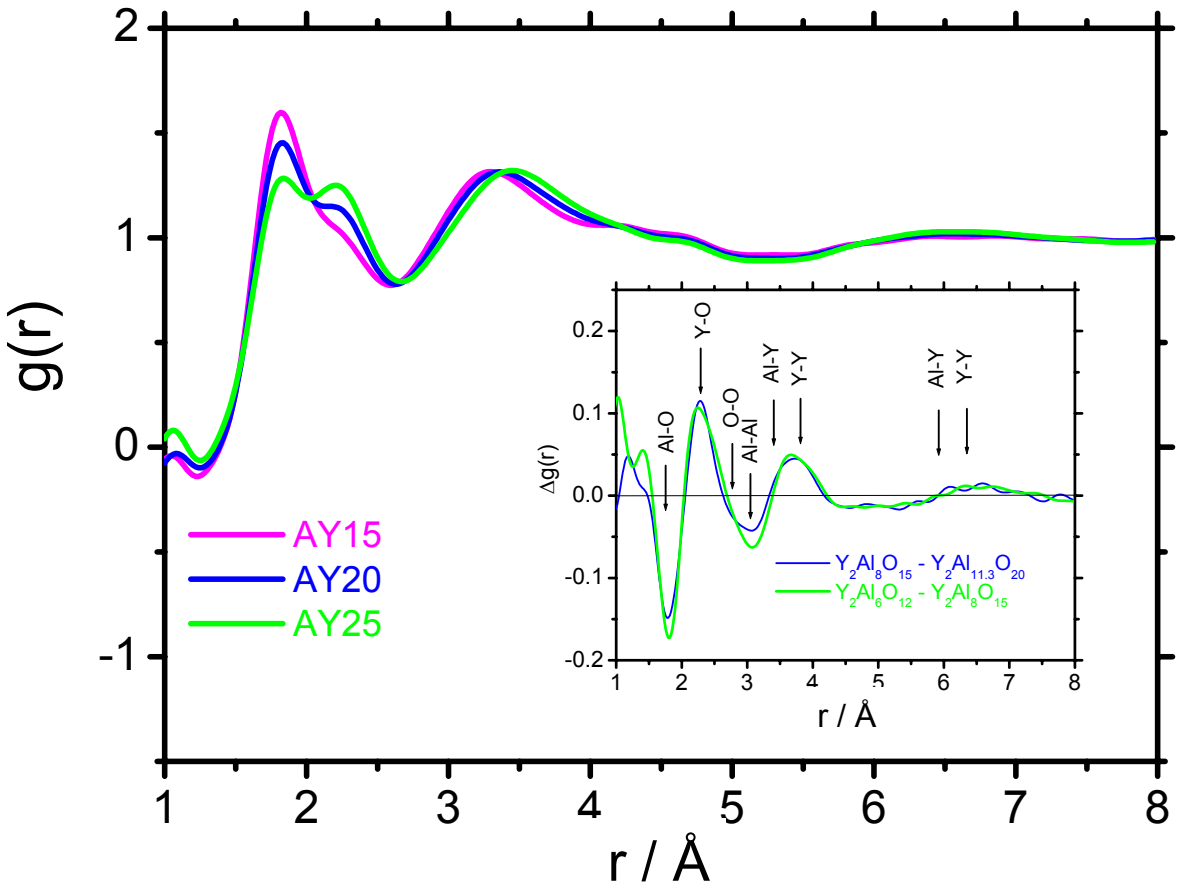
g(r)
r / Å
AY15
AY20
AY25
Δg(r)
Al-O
Y-O
O-O
Al-Al
Al-Y
Y-Y
Al-Y
Y-Y
$Y_2Al_8O_{15}$ - $Y_2Al_{11.3}O_{20}$
$Y_2Al_6O_{12}$ - $Y_2Al_8O_{15}$
r / Å

Figure 4